Computers and Fluids 231 (2021) 105151

Contents lists available at ScienceDirect

Computers and Fluids

journal homepage: www.elsevier.com/locate/compfluid

Dynamics of interfacial gravity–capillary waves in three-dimensional fluids of great depth

Haiyan Li [a,b], Zhan Wang [a,b,c,*]

[a] Institute of Mechanics, Chinese Academy of Sciences, Beijing 100190, China
[b] School of Engineering Science, University of Chinese Academy of Sciences, Beijing 100049, China
[c] School of Future Technology, University of Chinese Academy of Sciences, Beijing 100049, China

ARTICLE INFO

Keywords:
Isotropic model
ETD
Interfacial wave
Capillary–gravity wave

ABSTRACT

This paper proposes a new isotropic bidirectional model for weakly nonlinear gravity–capillary waves propagating between two incompressible, inviscid, and immiscible fluids of different densities. The newly developed equation is a generalization of the celebrated two-dimensional Benjamin equation. It is derived based on the nonlocal formulation of water wave (i.e., the Ablowitz–Fokas–Musslimani formulation) and computed with the modified exponential time-differencing method. It is found that horizontally two-dimensional, fully localized traveling waves (known as lumps) exist in the model equation, and plane solitary waves are unstable subject to long transverse perturbations, which evolve into groups of lumps in the long-term dynamics. When considering topographical disturbances on the rigid upper boundary, the nonlinear effect becomes important when a uniform flow passes beneath a locally confined topography with a near-critical speed, and the phenomenon of time-periodic shedding of lumps occurs. Unlike the near-critical situation, the subcritical flows usually generate steady elevation waves, while the supercritical ones produce a V-shaped pattern of wake lines. Furthermore, it is shown that a uniformly accelerated motion can also generate lumps provided that the flow stays in the transcritical regime for a considerably long time.

1. Introduction

Interfacial waves propagating along the interface between two homogeneous fluids of different densities have a wide range of applications in nature and industry. In the present work, we focus on nonlinear interfacial gravity–capillary waves in a three-dimensional two-layer fluid system. The upper layer is bounded above by a non-flat rigid wall, and the lower layer is of infinite depth. Gravity–capillary (GC) waves arise when the effects of gravity and surface tension are approximate, of equal importance. A new type of solitary wave was found in free-surface GC waves in deep water about three decades ago. These solutions feature oscillatory decaying tails and monotonically decaying envelopes, and hence termed wavepacket solitary waves. Theoretically, the existence of wavepacket solitary waves requires a global phase speed minimum at a finite wavenumber in the linear dispersion relation.

Studies on surface GC solitary waves date back to Longuet-Higgins [1] and Vanden-Broeck & Dias [2], who numerically found two fundamental branches (depression waves and elevation waves) on a two-dimensional fluid (corresponding to a one-dimensional free surface) of infinite depth. In three dimensions (with a two-dimensional free surface), fully localized traveling-wave solutions, commonly referred to as 'lumps', have received considerable attention in the past two decades. Of note is the work of Berger & Milewski [3] who studied the generation of lumps by a pressure forcing in a modified Benney–Luke equation, Părău et al. [4] who first computed GC lumps in the full Euler equations using a boundary integral equation method, Kim & Akylas [5] who provided sufficient conditions for the existence of lumps from an asymptotic point of view, Akers & Milewski [6] who proposed a weakly nonlinear unidirectional model and investigated the stability and dynamics of GC lumps, and Wang & Milewski [7,8] who proposed a quantitative model based on the series truncation of the Dirichlet–Neumann operator in the Hamiltonian framework and revisited the transverse instability of plane GC solitary waves which led to a new type of traveling waves (i.e., transversally periodic solitary waves). On the experimental side, depression GC lumps were first generated under controlled conditions by Diorio et al. [9], achieved by blowing air towards the surface of the fluid and moving the air source with speed close to the phase speed minimum. Similar experimental techniques were further used to investigate oblique collisions between lumps by

* Corresponding author at: Institute of Mechanics, Chinese Academy of Sciences, Beijing 100190, China.
E-mail address: zwang@imech.ac.cn (Z. Wang).

https://doi.org/10.1016/j.compfluid.2021.105151
Received 13 July 2021; Accepted 6 September 2021
Available online 27 September 2021

Masnadi & Duncan [10] and the transverse instability of plane solitary waves by Park & Cho [11].

The systematic study on interfacial GC waves was pioneered by Benjamin [12], who proposed a weakly nonlinear long-wave model for the scenario when a thin layer lies on top of an infinitely deep fluid of slightly higher density. In addition, Benjamin assumed a strong interfacial tension, which could suppress the Kelvin–Helmholtz instability [13]. The Benjamin equation was generalized to two spatial dimensions by Kim & Akylas [14] in the spirit of the Kadomtsev–Petviashvili (KP) equation, namely, a unidirectional model with slight inhomogeneity in the transverse direction. Both numerical and asymptotic features of the two-dimensional (2D) Benjamin equation were thoroughly investigated in [14]. These authors showed the existence of wavepacket lumps via a pseudo-spectral method and their algebraically decaying tails due to the wave-induced mean flow. Under the same scenario, linear stability analyses for plane solitary waves in the full Euler equations subject to longitudinal and transverse perturbations were carried out by Calvo & Akylas [15] and Kim [16], respectively. When both layers are of infinite depth, wavepacket solitary waves were also reported numerically in the full Euler equations for the horizontally one-dimensional problem by Laget & Dias [17] and in the reduced model equations for the horizontally two-dimensional problem by Wang et al. [18].

While anisotropic unidirectional models have been successful in many aspects of surface/interfacial wave problems, there are still some limitations. Firstly, they cannot correctly describe the two-way propagation of water waves, such as wave reflection/transmission across the media interface and head on collisions of solitary waves. Secondly, it is not suitable to use an anisotropic model to study wave phenomena whose transverse variations are similar to those in the primary direction of propagation, such as the Kelvin wake and oblique interactions between solitary waves. In the spirit of the Benney–Luke equation (see [19]), we derived an isotropic bidirectional model equation for interfacial GC waves under Benjamin's scenario. The newly developed model modifies the classic Benney–Luke equation by adding a linear pseudo-differential operator resulting from the existence of the lower layer. On the other hand, it is a generalization of the 2D Benjamin equation via loosing the scale constraints. Furthermore, we assume a time-dependent topography disturbance on the rigid upper boundary to study lump generation by a moving flow with a uniform speed/acceleration.

The rest of the paper is organized as follows. In Section 2, we present the derivation of the Benney–Luke-type model for interfacial waves between shallow and deep fluids based on the Ablowitz–Fokas–Musslimani formulation for water waves. A numerical algorithm based on a symmetric factorization of the linear part of the isotropic model, followed by the fourth-order Runge–Kutta exponential time differencing scheme, is proposed in Section 3. We apply this numerical procedure in Section 4 to study properties of interfacial GC waves, including the existence of wavepacket solitary waves, transverse instability of plane solitary waves, various types of collisions between lumps, and resonant responses caused by the localized topography disturbance on the rigid upper wall. Finally, a conclusion is given in Section 5.

2. Derivation

2.1. Mathematical formulation

Consider a three-dimensional incompressible and inviscid fluid system, composed by two immiscible layers with the lighter one being on top of the heavier one. Two fluids are separated by a sharp interface $z = \eta(x, y, t)$, where x and y are horizontal coordinates and the z-axis points upwards with $z = 0$ the undisturbed interface. The lower layer (denoted by D^-) is assumed to be semi-infinite, and the upper layer (denoted by D^+) is bounded on the top by impermeable wall $z = h + b(x, y, t)$ varying in space and time where $b(x, y, t)$ is a prescribed function (see the schematic description of the physical problem in Fig. 1). The density of the fluid in each layer is supposed to be constant denoted by ρ^+ and ρ^- with $\rho^+ < \rho^-$, where superscripts '+' and '−' refer to fluid properties associated with the upper and lower layers, respectively. The flow in each layer is supposed to be irrotational, and velocity potentials $\phi^\pm$ can be introduced which satisfy the Laplace equation in respective domains, namely

$$\begin{aligned} &\Delta\phi^+ + \phi^+_{zz} = 0, \qquad \text{for} \quad \eta(x,y,t) < z < h + b(x,y,t), \\ &\Delta\phi^- + \phi^-_{zz} = 0, \qquad \text{for} \quad z < \eta(x,y,t), \end{aligned} \tag{2.1}$$

where $\Delta = \partial_{xx} + \partial_{yy}$ is the two-dimensional horizontal Laplace operator. On the interface $z = \eta(x, y, t)$, the nonlinear kinematic and dynamic boundary conditions read:

$$\eta_t = \phi^-_z - \nabla\phi^- \cdot \nabla\eta = \phi^+_z - \nabla\phi^+ \cdot \nabla\eta, \tag{2.2}$$

$$\begin{aligned} 0 = {} & \rho^-\phi^-_t - \rho^+\phi^+_t + \frac{\rho^+}{2}\left[|\nabla\phi^+|^2 + (\phi^+_z)^2\right] - \frac{\rho^-}{2}\left[|\nabla\phi^-|^2 + (\phi^-_z)^2\right] \\ & + \sigma\nabla\cdot\left[\frac{\nabla\eta}{\sqrt{1+|\nabla\eta|^2}}\right], \end{aligned} \tag{2.3}$$

where ∇ and $\nabla\cdot$ are the horizontal gradient and horizontal divergent operators, respectively, g is the acceleration due to gravity, and σ is the surface tension coefficient. Finally, the boundary conditions

$$\phi^+_z - \nabla b \cdot \nabla\phi^+ = b_t, \quad \text{at} \quad z = h + b(x,y,t), \tag{2.4}$$

$$\phi^-_z \to 0, \quad \text{as} \quad z \to -\infty, \tag{2.5}$$

complete the whole system.

2.2. Ablowitz–Fokas–Musslimani formulation

Recently, Ablowitz et al. [20] introduced an explicit non-local formulation for the classical water-wave problem in two and three dimensions. It was later generalized to include the time-dependent bottom topography by Curtis & Shen [21] and to study interfacial waves in two-fluid systems by Haut & Ablowitz [22] and Yuan et al. [23]. In the subsequent analyzes, we briefly describe the Ablowitz–Fokas–Musslimani method and its generalization to the present problem. First of all, it is straightforward to verify that the following identity

$$0 = \left(\phi^\pm_z\psi_x + \phi^\pm_x\psi_z\right)_x + \left(\phi^\pm_z\psi_y + \phi^\pm_y\psi_z\right)_y + \left(\phi^\pm_z\psi_z - \phi^\pm_x\psi_x - \phi^\pm_y\psi_y\right)_z \tag{2.6}$$

holds for arbitrary harmonic function ψ. Applying the divergence theorem to Eq. (2.6) in the upper layer, one obtains

$$\begin{aligned} 0 = {} & \int \Big[-b_x\left(\phi^+_z\psi_x + \phi^+_x\psi_z\right) - b_y\left(\phi^+_z\psi_y + \phi^+_y\psi_z\right) \\ & + \left(\phi^+_z\psi_z - \nabla\phi^+\cdot\nabla\psi\right)\Big]_{z=h+b}\,\mathrm{d}\mathbf{r} \\ & + \int \Big[\eta_x\left(\phi^+_z\psi_x + \phi^+_x\psi_z\right) + \eta_y\left(\phi^+_z\psi_y + \phi^+_y\psi_z\right) \\ & - \left(\phi^+_z\psi_z - \nabla\phi^+\cdot\nabla\psi\right)\Big]_{z=\eta}\,\mathrm{d}\mathbf{r}, \end{aligned} \tag{2.7}$$

where $\mathbf{r} = (x, y)^\top$ is the vector of horizontal coordinates. Substituting $\psi = e^{\mathrm{i}\mathbf{k}\cdot\mathbf{r}+kz}$ into Eq. (2.7) yields

$$0 = \int e^{\mathrm{i}\mathbf{k}\cdot\mathbf{r}+k(\eta-h)}\left(-k\eta_t + \mathrm{i}\mathbf{k}\cdot\nabla\boldsymbol{\Phi}^+\right)\mathrm{d}\mathbf{r} + \int e^{\mathrm{i}\mathbf{k}\cdot\mathbf{r}+kb}\left(kb_t - \mathrm{i}\mathbf{k}\cdot\nabla\boldsymbol{\Phi}^b\right)\mathrm{d}\mathbf{r}, \tag{2.8}$$

where $\mathbf{k} = (k_x, k_y)^\top$ is the wavenumber vector, $k = \sqrt{k_x^2 + k_y^2}$ is its modulus, and the velocity potentials on two boundaries are denoted by $\boldsymbol{\Phi}^+ = \phi^+(x, y, \eta, t)$ and $\boldsymbol{\Phi}^b = \phi^+(x, y, b, t)$, respectively. Upon noting that

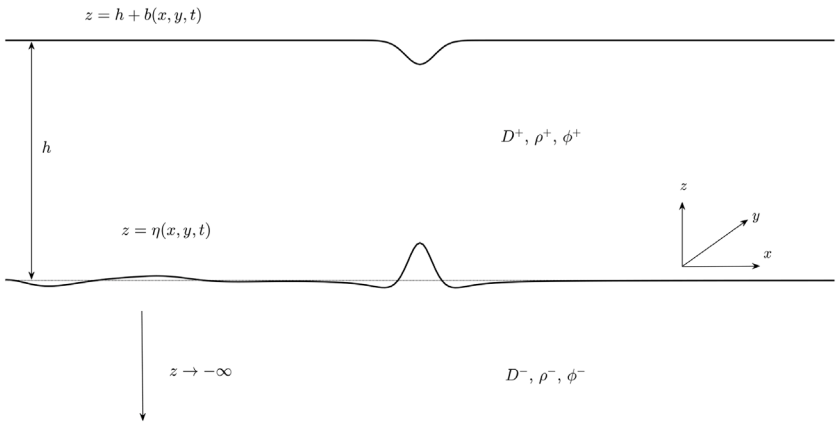

Fig. 1. Schematic description of the physical problem.

$e^{\mathrm{i}\mathbf{k}\cdot\mathbf{r}-kz}$ is also a solution to the Laplace equation, it is easy to verify that

$$0 = \int e^{\mathrm{i}\mathbf{k}\cdot\mathbf{r}-k(\eta-h)}\left(k\eta_t + \mathrm{i}\mathbf{k}\cdot\nabla\boldsymbol{\Phi}^+\right)\mathrm{d}\mathbf{r} - \int e^{\mathrm{i}\mathbf{k}\cdot\mathbf{r}-kb}\left(kb_t + \mathrm{i}\mathbf{k}\cdot\nabla\boldsymbol{\Phi}^b\right)\mathrm{d}\mathbf{r}\,. \tag{2.9}$$

Adding and subtracting Eqs. (2.8) and (2.9), one then obtains

$$\begin{aligned} 0 = \int e^{\mathrm{i}\mathbf{k}\cdot\mathbf{r}}\big[&-k\sinh(k(\eta-h))\eta_t + \mathrm{i}\mathbf{k}\cdot\nabla\boldsymbol{\Phi}^+\cosh(k(\eta-h)) \\ &+ k\sinh(kb)b_t - \mathrm{i}\mathbf{k}\cdot\nabla\boldsymbol{\Phi}^b\cosh(kb)\big]\mathrm{d}\mathbf{r} \end{aligned} \tag{2.10}$$

and

$$\begin{aligned} 0 = \int e^{\mathrm{i}\mathbf{k}\cdot\mathbf{r}}\Big[&-\cosh(k(\eta-h))\eta_t + \mathrm{i}\mathbf{k}\cdot\nabla\boldsymbol{\Phi}^+\frac{\sinh(k(\eta-h))}{k} \\ &+ \cosh(kb)b_t - \mathrm{i}\mathbf{k}\cdot\nabla\boldsymbol{\Phi}^b\frac{\sinh(kb)}{k}\Big]\mathrm{d}\mathbf{r}\,. \end{aligned} \tag{2.11}$$

In the same vein, one can obtain the global relation for the lower layer as

$$0 = \int e^{\mathrm{i}\mathbf{k}\cdot\mathbf{r}}\left(k\eta_t - \mathrm{i}\mathbf{k}\cdot\nabla\boldsymbol{\Phi}^-\right)e^{k\eta}\,\mathrm{d}\mathbf{r}\,, \tag{2.12}$$

where $\boldsymbol{\Phi}^- = \phi^-(x, y, \eta, t)$. If we denote by $R = \rho^-/\rho^+ > 1$ the density ratio, then the dynamic boundary condition on the interface can be rewritten as

$$\begin{aligned} 0 =&(\boldsymbol{\Phi}^+ - R\boldsymbol{\Phi}^-)_t - (R-1)g\eta + \frac{1}{2}|\nabla\boldsymbol{\Phi}^+|^2 - \frac{R}{2}|\nabla\boldsymbol{\Phi}^-|^2 - \frac{(\eta_t + \nabla\eta\cdot\nabla\boldsymbol{\Phi}^+)^2}{2(1+|\nabla\eta|^2)} \\ &+ \frac{R(\eta_t + \nabla\eta\cdot\nabla\boldsymbol{\Phi}^-)^2}{2(1+|\nabla\eta|^2)} + \frac{\sigma}{\rho^+}\nabla\cdot\left[\frac{\nabla\eta}{\sqrt{1+|\nabla\eta|^2}}\right]. \end{aligned} \tag{2.13}$$

To continue the derivation, we introduce the Boussinesq scaling

$$x, y \sim L\,, \qquad b, \eta \sim a\,, \qquad t \sim \frac{L}{\sqrt{gh(R-1)}}\,, \qquad \boldsymbol{\Phi}^{\pm,b} \sim \frac{agL\sqrt{R-1}}{\sqrt{gh}}\,,$$

where L is typical length scale in horizontal directions and a stands for the characteristic wave amplitude. Small parameters $\epsilon = a/h$ and $\mu = h/L$ are introduced to measure the nonlinearity and dispersion, respectively, and in addition, we assume these two parameters are of the same order, namely $\epsilon = O(\mu)$. After nondimensionalization, the global relations (2.10)–(2.12) read

$$\begin{aligned} 0 = &\int e^{\mathrm{i}\mathbf{k}\cdot\mathbf{r}}\left[-\mu k\sinh(\mu k(\epsilon\eta-1))\eta_t + \mathrm{i}\mathbf{k}\cdot\nabla\boldsymbol{\Phi}^+\cosh(\mu k(\epsilon\eta-1))\right]\mathrm{d}\mathbf{r} \\ &+ \int e^{\mathrm{i}\mathbf{k}\cdot\mathbf{r}}\left[\mu k\sinh(\epsilon\mu kb)b_t - \mathrm{i}\mathbf{k}\cdot\nabla\boldsymbol{\Phi}^b\cosh(\epsilon\mu kb)\right]\mathrm{d}\mathbf{r}\,, \end{aligned} \tag{2.14}$$

$$\begin{aligned} 0 = &\int e^{\mathrm{i}\mathbf{k}\cdot\mathbf{r}}\left[-\cosh(\mu k(\epsilon\eta-1))\eta_t + \mathrm{i}\mathbf{k}\cdot\nabla\boldsymbol{\Phi}^+\frac{\sinh(\mu k(\epsilon\eta-1))}{\mu k}\right]\mathrm{d}\mathbf{r} \\ &+ \int e^{\mathrm{i}\mathbf{k}\cdot\mathbf{r}}\left[\cosh(\epsilon\mu kb)b_t - \mathrm{i}\mathbf{k}\cdot\nabla\boldsymbol{\Phi}^b\frac{\sinh(\epsilon\mu kb)}{\mu k}\right]\mathrm{d}\mathbf{r}\,, \end{aligned} \tag{2.15}$$

and

$$0 = \int e^{\mathrm{i}\mathbf{k}\cdot\mathbf{r}}\left(\mu k\eta_t - \mathrm{i}\mathbf{k}\cdot\nabla\boldsymbol{\Phi}^-\right)e^{\epsilon\mu k\eta}\,\mathrm{d}\mathbf{r}\,. \tag{2.16}$$

While the dynamic boundary condition becomes

$$\begin{aligned} 0 = &(\boldsymbol{\Phi}^+ - R\boldsymbol{\Phi}^-)_t - \eta + \frac{\epsilon}{2}|\nabla\boldsymbol{\Phi}^+|^2 - \frac{\epsilon R}{2}|\nabla\boldsymbol{\Phi}^-|^2 - \frac{\epsilon\mu^2}{2}\frac{(\eta_t + \epsilon\nabla\eta\cdot\nabla\boldsymbol{\Phi}^+)^2}{1+\epsilon^2\mu^2|\nabla\eta|^2} \\ &+ \frac{\epsilon\mu^2 R}{2}\frac{(\eta_t + \epsilon\nabla\eta\cdot\nabla\boldsymbol{\Phi}^-)^2}{1+\epsilon^2\mu^2|\nabla|^2} + B\mu^2\nabla\cdot\left[\frac{\nabla\eta}{\sqrt{1+\epsilon^2\mu^2|\nabla\eta|^2}}\right], \end{aligned} \tag{2.17}$$

where $B = \sigma/(\rho^- - \rho^+)gh^2$ is called the Bond number for interfacial waves. In the present context, we assume $B \gg 1$ ($\sim 1/\mu$), an assumption first used by Benjamin [12] and later on generalized by Kim & Akylas [14] and Haut & Ablowitz [22] among others. Taking the Maclaurin series expansions for the global relations and retaining terms valid up to $O(\epsilon, \mu)$, we have

$$0 = \int e^{\mathrm{i}\mathbf{k}\cdot\mathbf{r}}\left(\mathrm{i}\mathbf{k}\cdot\nabla\boldsymbol{\Phi}^+ - \mathrm{i}\mathbf{k}\cdot\nabla\boldsymbol{\Phi}^b\right)\mathrm{d}\mathbf{r}\,, \tag{2.18}$$

$$0 = \int e^{\mathrm{i}\mathbf{k}\cdot\mathbf{r}}\left[-\eta_t + \mathrm{i}\mathbf{k}\cdot\nabla\boldsymbol{\Phi}^+(\epsilon\eta-1) + b_t - \mathrm{i}\mathbf{k}\cdot\nabla\boldsymbol{\Phi}^b(\epsilon b)\right]\mathrm{d}\mathbf{r}\,, \tag{2.19}$$

$$0 = \int e^{\mathrm{i}\mathbf{k}\cdot\mathbf{r}}\left(\mu k\eta_t - \mathrm{i}\mathbf{k}\cdot\nabla\boldsymbol{\Phi}^-\right)\mathrm{d}\mathbf{r}\,. \tag{2.20}$$

Similarly, one can obtain the approximation of the dynamic boundary condition

$$(\boldsymbol{\Phi}^+ - R\boldsymbol{\Phi}^-)_t - \eta + \frac{\epsilon}{2}|\nabla\boldsymbol{\Phi}^+|^2 - \frac{\epsilon R}{2}|\nabla\boldsymbol{\Phi}^-|^2 + B\mu^2\Delta\eta = 0\,. \tag{2.21}$$

Upon noting $\mathrm{i}\mathbf{k} \sim -\nabla$ and $k^2 \sim -\Delta$, we can translate the global relations (2.18)–(2.20) to pseudo-differential equations based on the inverse Fourier transform. The integral (2.18) implies $\boldsymbol{\Phi}^b = \boldsymbol{\Phi}^+$ therefore we

can decouple Φ^b from the system. While the integrals (2.19) and (2.20) can be recast to

$$\eta_t = \Delta\Phi^+ + b_t - \epsilon\nabla\cdot\eta\nabla\Phi^+ + \epsilon\nabla\cdot b\nabla\Phi^b\,, \tag{2.22}$$

$$\eta_t = (-\Delta)^{1/2}\Phi^-/\mu\,. \tag{2.23}$$

If we denote by $\xi = \Phi^+ - R\Phi^-$ the potential jump across the interface, then combining Eqs. (2.22) and (2.23) yields

$$\Phi^+ = \xi + \mu R(-\Delta)^{-1/2}(\Delta\xi + b_t) + O(\epsilon\mu, \mu^2)\,. \tag{2.24}$$

Taking the time derivative of Eq. (2.21) and replacing η_t with Eq. (2.22), one arrives at

$$\begin{aligned}&\xi_{tt} - \Delta\Phi^+ - b_t + \epsilon\nabla\cdot\eta\nabla\Phi^+ - \epsilon\nabla\cdot b\nabla\Phi^+\\ &\quad + \frac{\epsilon}{2}|\nabla\Phi^+|_t^2 + B\mu^2\Delta(\Delta\Phi^+ + b_t) = 0\,.\end{aligned} \tag{2.25}$$

To eliminate Φ^+ and η, we substitute Eq. (2.24) into Eq. (2.25) and replace η with ξ_t. It then follows that

$$\begin{aligned}0 = {}&\xi_{tt} - \Delta\xi - \mu R(-\Delta)^{3/2}\xi + B\mu^2\Delta^2\xi + \epsilon\left(|\nabla\xi|_t^2 + \xi_t\Delta\xi\right)\\ &- b_t + \mu R(-\Delta)^{1/2}b_t + B\mu^2\Delta b_t - \epsilon\nabla\cdot b\nabla\xi\,.\end{aligned} \tag{2.26}$$

Eq. (2.26) is an isotropic model describing bidirectional propagation of interfacial GC waves. It modifies the classic Benney–Luke equation by adding a linear non-local term when the topographic effect is neglected (i.e. $b = 0$). It is also noted that Eq. (2.26) reduces to the 2D Benjamin equation in the unidirectional and quasi-three-dimensional approximation, but we omit the detailed derivation here.

A modification of Eq. (2.26) is usually required to regularize the linear dispersion relation. Upon noting that $\Delta\xi = \xi_{tt} - b_t + O(\epsilon, \mu)$, Eq. (2.26) can be rewritten as

$$\begin{aligned}0 = {}&\left[1 + \mu R(-\Delta)^{1/2}\right]\xi_{tt} - \Delta\xi + B\mu^2\Delta^2\xi + \epsilon\left(|\nabla\xi|_t^2 + \xi_t\Delta\xi\right)\\ &- b_t + B\mu^2\Delta b_t - \epsilon\nabla\cdot b\nabla\xi\,.\end{aligned} \tag{2.27}$$

Eq. (2.27) is the primary model used in the subsequent computations. We shall henceforth call this the Benjamin–Benney–Luke (BBL) equation.

3. Numerical method

The exponential time differencing method (ETD) is a class of time-discretization schemes for solving nonlinear evolution equations. The fundamental idea is to perform exact integration of the governing equations followed by an approximation of the integral involving the nonlinear terms [24]. It was originally used in the field of computational electrodynamics and the interested readers are referred to [25] for a comprehensive review. Cox and Matthews [25] first derived explicit ETD schemes of arbitrary order and combined them with the Runge–Kutta method, which was then termed the 'ETDRK' method. Kassam & Trefethen [26] systematically compared numerical solutions of the ETDRK scheme with the competing methods of implicit–explicit differencing, integrating factors, time-splitting, and Fornberg and Driscoll's 'slider' for four PDEs in a one-dimensional domain: the Korteweg–de Vries, Kuramoto–Sivashinsky, Burgers', and Allen–Cahn equations. Their numerical results suggested that the ETD scheme generally outperformed the others in solving stiff PDEs. There are relatively fewer studies on applications of the ETD scheme to spatially two-dimensional problems. Of note is the work of Hoz & Vadillo [27] who applied the ETD scheme to the '2+1' nonlinear Schrödinger equation and Asgari & Hosseini [28] who focused on the '2+1' nonlinear sine–Gordon equation. However, the ETD method has barely been combined with free-surface or interfacial wave problems.

In the present work, we extend the ETDRK method to the interfacial wave problem, i.e., the bidirectional model (2.27). In the following we briefly sketch the numerical scheme for solving a second-order nonlinear dispersive wave equation. We first write the PDE in an abstract form

$$\xi_{tt} + \mathcal{L}^2\xi = \mathcal{N}(\xi, \xi_t, t)\,, \tag{3.1}$$

where $\xi(x, y, t)$ is a real function, $\mathcal{L}^2$ is a non-negative linear operator normally involving spatial derivatives, and $\mathcal{N}$ includes nonlinear and forcing terms. Following Milewski & Tabak [29], we factor the linear part of Eq. (3.1) which yields

$$\left(\frac{\partial}{\partial t} - \mathrm{i}\mathcal{L}\right)\left(\frac{\partial}{\partial t} + \mathrm{i}\mathcal{L}\right)\xi = \mathcal{N}(\xi, \xi_t, t)\,. \tag{3.2}$$

Introducing $u = \xi_t + \mathrm{i}\mathcal{L}\xi$ gives $\xi_t = \mathrm{Re}(u)$ and $\mathcal{L}\xi = \mathrm{Im}(u)$, and Eq. (3.2) can be rewritten as

$$u_t - \mathrm{i}\mathcal{L}u = \mathcal{N}(u, t)\,. \tag{3.3}$$

Assuming that Eq. (3.1) is subject to spatially periodic boundary conditions, it is natural to numerically solve the equation via the standard pseudo-spectral method. Taking the Fourier transform of Eq. (3.3) in spatial variables yields

$$\hat{u}_t - \mathrm{i}\hat{\mathcal{L}}\hat{u} = \hat{\mathcal{N}}(\hat{u}, t)\,, \tag{3.4}$$

where the dependence of Fourier coefficients on the wavenumber (k_x, k_y) has been suppressed for ease of notations. We integrate Eq. (3.4) from t_n to t_{n+1} by using the method of integrating factors, which yields

$$\hat{u}(t_{n+1}) = e^{\mathrm{i}\hat{\mathcal{L}}h}\hat{u}(t_n) + e^{\mathrm{i}\hat{\mathcal{L}}h}\int_0^h e^{-\mathrm{i}\hat{\mathcal{L}}\tau}\hat{\mathcal{N}}\left(\hat{u}(t_n+\tau), t_n+\tau\right)\mathrm{d}\tau\,, \tag{3.5}$$

where $h = t_{n+1} - t_n$ is the time step. The formula (3.5) is exact and the key is to find a good numerical approximation for the integrand. In this respect, a pioneering work was due to Cox & Matthews [25] who used a generating function to obtain a sequence of recurrence formulae that could provide arbitrary order polynomial approximations of the integrand. Furthermore, they combined the ETD method with the Runge–Kutta scheme and generalized it to non-diagonal operators. Based on their results, in the current paper we use the ETD method coupled with the fourth-order Runge–Kutta scheme for time-stepping, which is termed the ETDRK4 hereafter. The numerical scheme can be expressed as follows:

$$\begin{aligned}a_n &= e^{\mathrm{i}\hat{\mathcal{L}}h/2}\hat{u}_n + \left(\mathrm{i}\hat{\mathcal{L}}\right)^{-1}\left(e^{\mathrm{i}\hat{\mathcal{L}}h/2} - 1\right)\hat{\mathcal{N}}(\hat{u}_n, t_n)\,,\\ b_n &= e^{\mathrm{i}\hat{\mathcal{L}}h/2}\hat{u}_n + \left(\mathrm{i}\hat{\mathcal{L}}\right)^{-1}\left(e^{\mathrm{i}\hat{\mathcal{L}}h/2} - 1\right)\hat{\mathcal{N}}(a_n, t_n + h/2)\,,\\ c_n &= e^{\mathrm{i}\hat{\mathcal{L}}h/2}a_n + \left(\mathrm{i}\hat{\mathcal{L}}\right)^{-1}\left(e^{\mathrm{i}\hat{\mathcal{L}}h/2} - 1\right)\left[2\hat{\mathcal{N}}(b_n, t_n + h/2) - \hat{\mathcal{N}}(\hat{u}_n, t_n)\right]\,,\\ \hat{u}_{n+1} &= e^{\mathrm{i}\hat{\mathcal{L}}h}\hat{u}_n + \alpha\hat{\mathcal{N}}(\hat{u}_n, t_n) + 2\beta\left[\hat{\mathcal{N}}(a_n, t_n + h/2) + \hat{\mathcal{N}}(b_n, t_n + h/2)\right]\\ &\quad + \gamma\hat{\mathcal{N}}(c_n, t_n + h/2)\,,\end{aligned} \tag{3.6}$$

where $\hat{u}_n$ is short for $\hat{u}(t_n)$, and α, β, γ are coefficients given by

$$\alpha = h^{-2}\left(\mathrm{i}\hat{\mathcal{L}}\right)^{-3}\left[-4 - \mathrm{i}\hat{\mathcal{L}}h + e^{\mathrm{i}\hat{\mathcal{L}}h}\left(4 - 3\mathrm{i}\hat{\mathcal{L}}h + \left(\mathrm{i}\hat{\mathcal{L}}h\right)^2\right)\right]\,, \tag{3.7}$$

$$\beta = h^{-2}\left(\mathrm{i}\hat{\mathcal{L}}\right)^{-3}\left[2 + \mathrm{i}\hat{\mathcal{L}}h + e^{\mathrm{i}\hat{\mathcal{L}}h}\left(-2 + \mathrm{i}\hat{\mathcal{L}}h\right)\right]\,, \tag{3.8}$$

$$\gamma = h^{-2}\left(\mathrm{i}\hat{\mathcal{L}}\right)^{-3}\left[-4 - 3\mathrm{i}\hat{\mathcal{L}}h - \left(\mathrm{i}\hat{\mathcal{L}}h\right)^2 + e^{\mathrm{i}\hat{\mathcal{L}}h}\left(4 - \mathrm{i}\hat{\mathcal{L}}h\right)\right]\,. \tag{3.9}$$

It should be pointed out that the coefficients given by (3.7)–(3.9) are not singular when $\hat{\mathcal{L}} = 0$ considering cancellations in their Taylor expansions. Finally, it is worth mentioning that the expressions of $\hat{\xi}$ and $\hat{\xi}_t$ can be recovered as

$$\hat{\xi}(k_x, k_y, t) = \frac{\hat{u}(k_x, k_y, t) - \hat{u}^*(-k_x, -k_y, t)}{\mathrm{i}\left[\hat{\mathcal{L}}(k_x, k_y) + \hat{\mathcal{L}}^*(-k_x, -k_y)\right]}\,, \tag{3.10}$$

$$\hat{\xi}_t(k_x, k_y, t) = \frac{\hat{\mathcal{L}}^*(-k_x, -k_y)\hat{u}(k_x, k_y, t) + \hat{\mathcal{L}}(k_x, k_y)\hat{u}^*(-k_x, -k_y, t)}{\hat{\mathcal{L}}(k_x, k_y) + \hat{\mathcal{L}}^*(-k_x, -k_y)}\,, \tag{3.11}$$

where the asterisk denotes complex conjugation. For the BBL equation, $\hat{\mathcal{L}}(0,0)$=0 and hence $\hat{\xi}(0,0,t)$ cannot be recovered from Eq. (3.10). Instead, $\hat{\xi}(0,0,t)$ should be updated numerically by integrating Eq. (3.11).

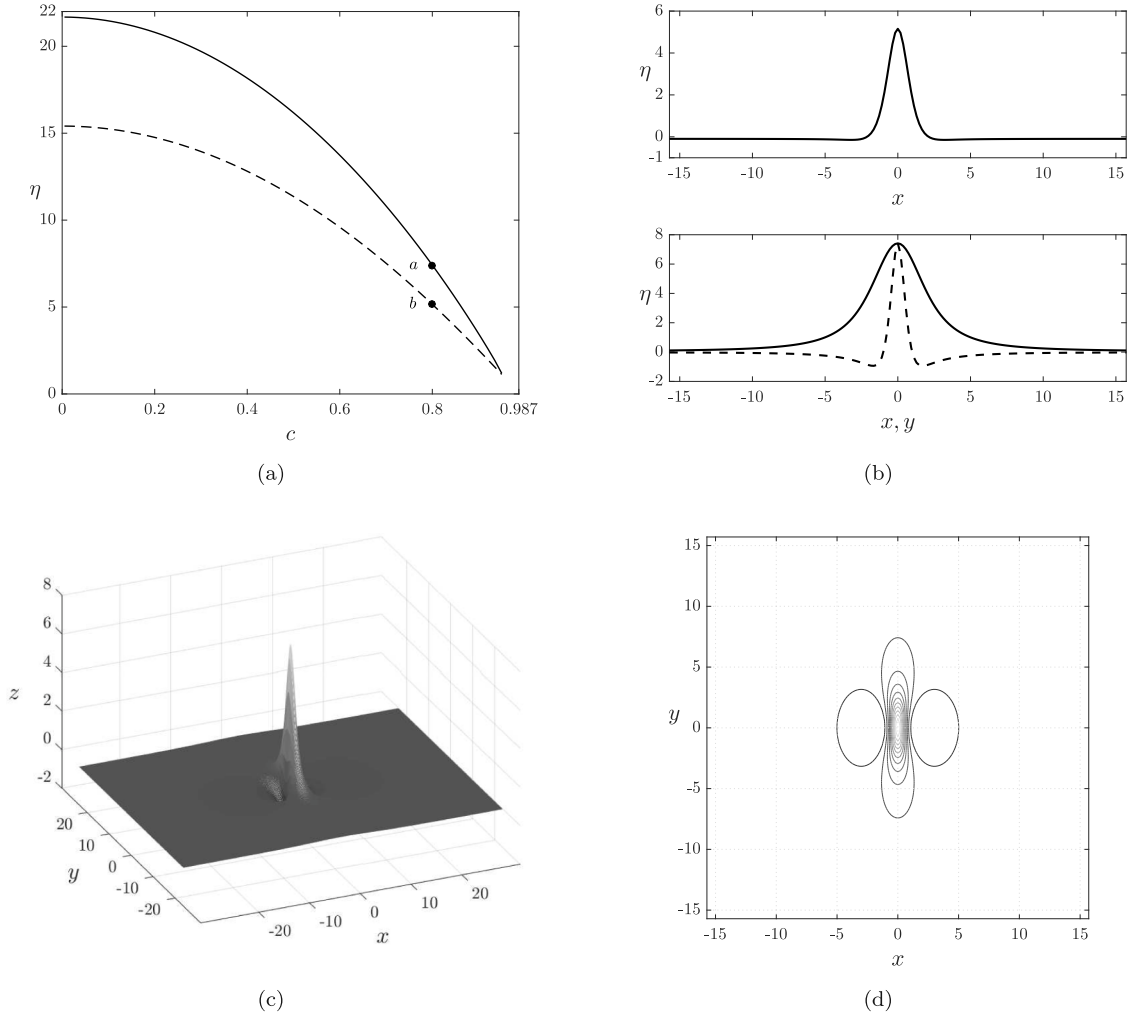

Fig. 2. (a) Bifurcation diagrams of plane solitary waves (dashed curve) and lumps (solid curve) in Eq. (4.1), both of which bifurcate from infinitesimal periodic waves at $c \approx 0.987$. Here $\epsilon = 0.1$, $\mu = 0.1$, $B = 10$, and $R = 1.05$ are used. (b) The top one is the x-cross-section of the plane solitary wave corresponding to 'b' on the bifurcation curve ($c = 0.8$, $\eta(0,0) = 5.156$), and the bottom one is the x-cross-section (dashed curve) and y-cross-section (solid curve) of the lump corresponding to 'a' on the bifurcation curve ($c = 0.8$, $\eta(0,0) = 7.4124$). (c) Wave profile of the lump. (d) Contour plot of the lump.

4. Results

4.1. Existence of solitary waves

There exist both plane solitary waves (1D solitary waves trivially extended in the transverse direction) and lumps (traveling waves that are localized in all horizontal directions) when gravity and surface tension are equally important. The existence of lumps in nonlinear dispersive equations has been confirmed by exact solutions of the KP-I equation, and numerical results of the Benney–Luke equation [3], the 2D Benjamin equation [14], and the full Euler equations [4], among others. Since Eq. (2.27) is a generalization of the 2D Benjamin equation, it is natural to search for free lumps in the BBL equation. For this purpose, the Petviashvili method is applied for computations. The basic principle behind the method is to convert the governing equation into Fourier space supplemented by a normalization factor upon the degree of nonlinearity, which can effectively prevent the numerical scheme from diverging (see also [20]). Assuming a lump propagates with speed c in the x-direction, that is to say, $\xi(x, y, t) = \xi(x - ct, y)$, and applying the Fourier transform to Eq. (2.27) with $b = 0$, one obtains

$$\hat{\xi} = \frac{\epsilon c \left(ik_x \widehat{|\nabla \xi|^2} + \widehat{\xi_x \Delta \xi} \right)}{-c^2 k^2 (1 + \mu R k) + k^2 + B\mu^2 k^4} \triangleq \mathcal{G}\left[\hat{\xi}\right] , \tag{4.1}$$

where 'hat' denotes the Fourier transform and k is the modulus of the wavenumber vector. To prevent unlimited increase or decrease of the modulus of $\hat{\xi}$, a multiplier needs to be introduced in every iteration step (see [20] for example). Finally, the iteration scheme reads

$$\hat{\xi}_{n+1} = \alpha_n \mathcal{G}[\hat{\xi}_n] \quad \text{with} \quad \alpha_n = \frac{\iint |\hat{\xi}_n|^2 \mathrm{d}k_x \mathrm{d}k_y}{\iint \hat{\xi}_n^* \mathcal{G}[\hat{\xi}_n] \mathrm{d}k_x \mathrm{d}k_y} . \tag{4.2}$$

Considering the insensitivity of the numerical scheme to initial data, a Gaussian type function is selected as the initial guess of wave profile in the numerical procedure.

Fig. 2 shows the bifurcation diagrams for both plane solitary waves and lumps as well as typical wave profiles. The 'speed–amplitude' bifurcation curves in Fig. 2(a) indicate that both plane solitary waves (dashed curve) and lumps (solid curve) bifurcate at $c \approx 0.987$ and feature a monotonic decreasing behavior. In contrast to the Benjamin

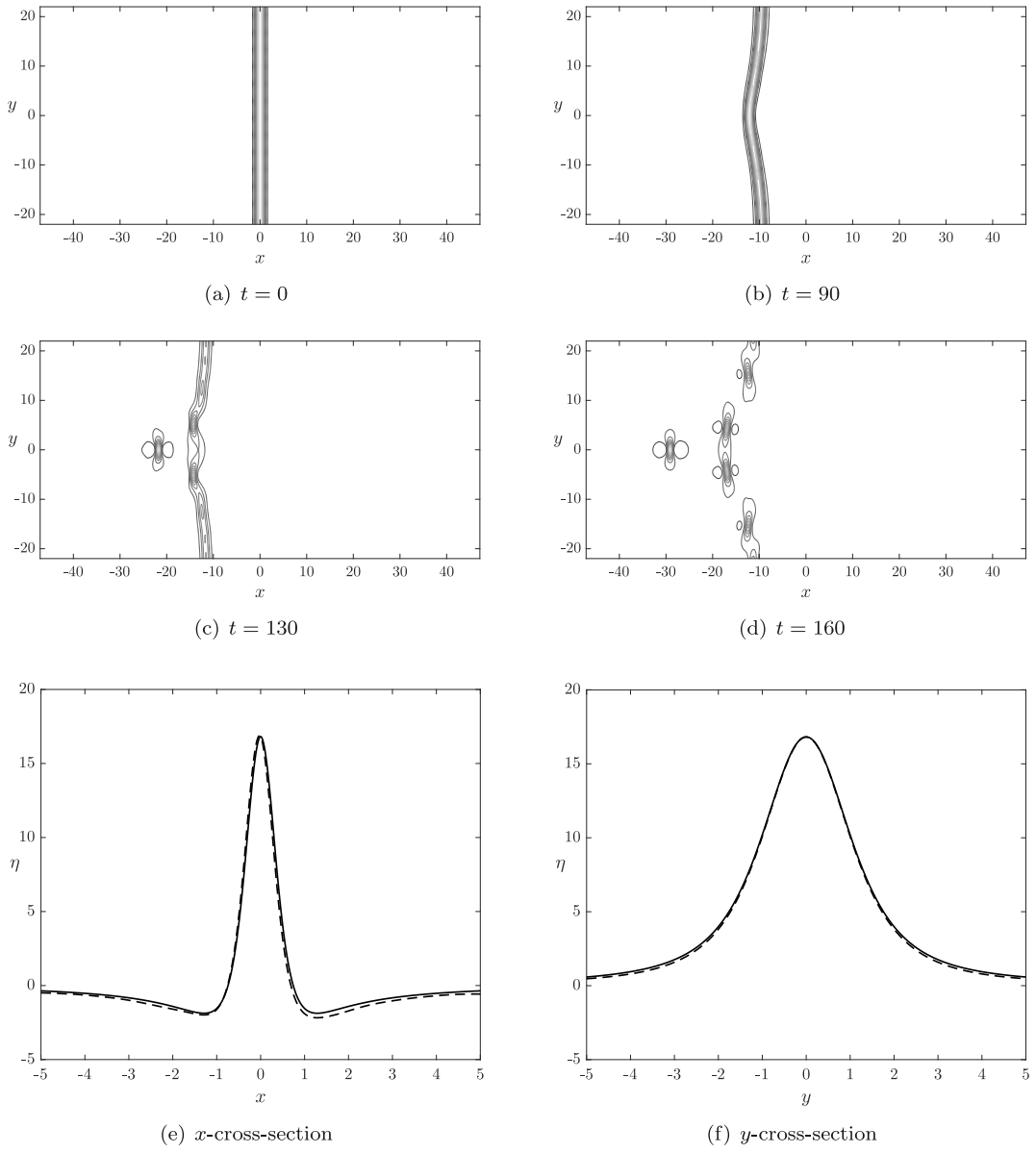

Fig. 3. (a–c) Time evolution of a plane solitary wave (shown in Fig. 2(b)) subject to a long transverse perturbation shows the emergence of a stable lump with speed $c \approx 0.47$. The disturbance is shown in a frame moving to the right with the speed of the undisturbed plane solitary wave. (d) The formation of a group of lumps. (e, f) Comparison of the lump emerged from the transverse instability (dash curve) with the exact traveling-wave solution (solid curve) for: (e) x-cross-section and (f) y-cross-section.

equation which admits both elevation and depression types of solitary waves (see [14,15] for details), only elevation waves which feature a positive displacement at their center are found in Eq. (4.1) for positive c. The x-cross-section of a plane solitary wave (corresponding to the point 'b' in 2(a)) and the x- and y-cross-sections of a lump (corresponding to the point 'a' in 2(a)) are plotted in 2(b). Finally, the lump's profile and contour plot are displayed in 2(c) and 2(d), respectively.

4.2. Transverse instability

The transverse instability of plane solitary waves is a classic problem. Kadomtsev & Petviashvili [30] first demonstrated that when surface tension is strong, the KdV solitons are unstable subject to transverse perturbations and evolve into lumps. A general criterion for the long-wave transverse instability of plane solitary waves was established by Bridges [31]. Kim & Akylas [14] studied the transverse instability of interfacial GC plane solitary waves via asymptotic analysis and numerical simulation in the framework of the 2D Benjamin equation. Kim [16] further generalized the result to the full Euler equations based on a linear analysis.

Motivated by the results in the 2D Benjamin equation, we check the transverse instability of plane elevation solitary waves for the model (2.27) in the absence of topography (i.e. $b = 0$). By virtue of the EDTRK4 method proposed in Section 3, we numerically integrate Eq. (2.27) in a periodic box of $30\pi \times 15\pi$ with 512×256 Fourier modes along the propagating and transverse directions, respectively, and apply the de-aliased technique with a doubling of Fourier modes to eliminate aliasing errors. The parameters are chosen as $\epsilon = 0.1$, $\mu = 0.1$, $B = 10$, and $R = 1.05$, with the time step of $\Delta t = 0.01$. A typical example is shown in Fig. 3. The initial condition in the experiment is taken as the

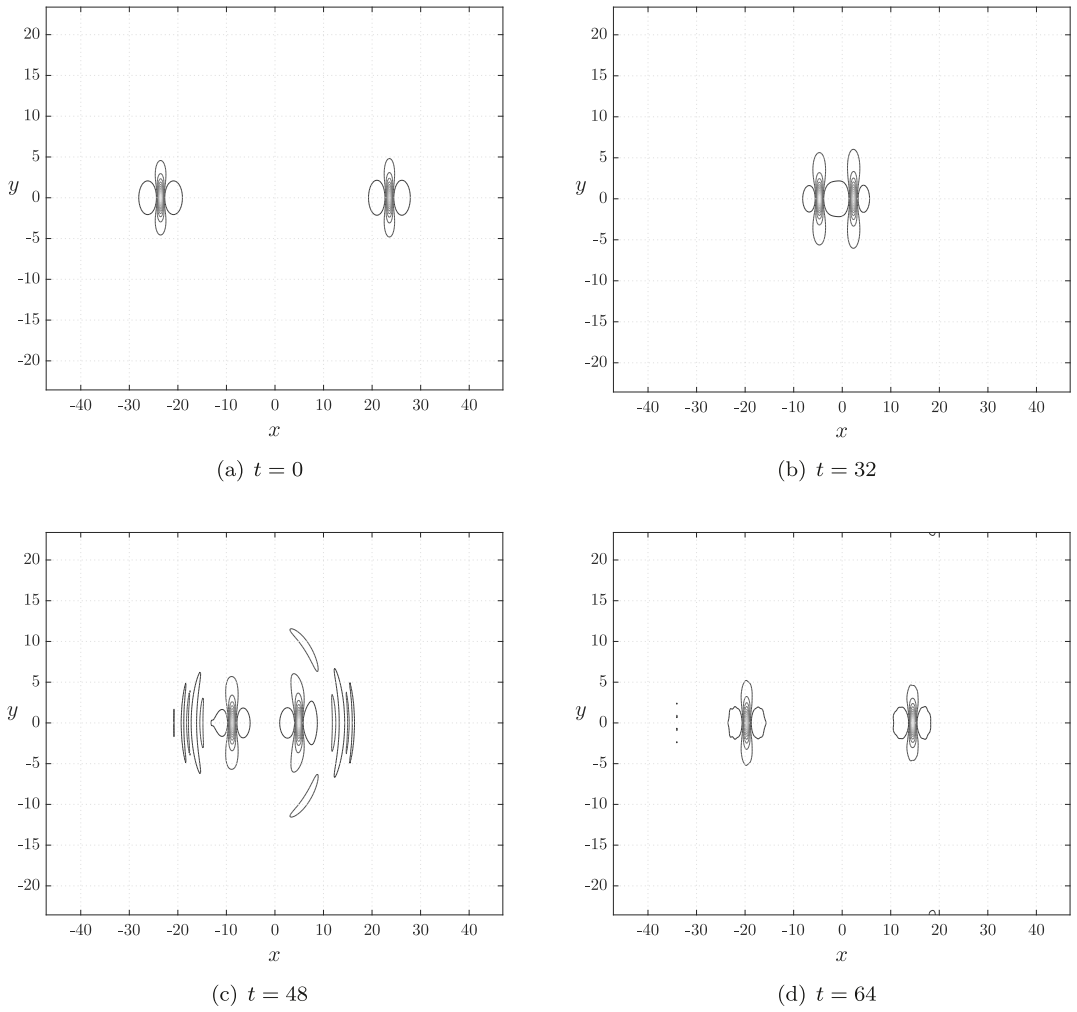

Fig. 4. Snapshots of a head-on collision of lumps. The initial data are prepared by superposing two different lumps traveling in opposite directions with the left one characterized by $c = 0.59$, $\|\eta\|_\infty = 13.99$ and the right one by $c = 0.665$, $\|\eta\|_\infty = 11.89$. After the collision, the amplitudes of lumps are 11.41 (left) and 13.66 (right) at $t = 64$.

form

$$\xi(x, y, t = 0) = \zeta(x)\left[1 + 0.01\cos\left(\frac{2y}{15}\right)\right], \tag{4.3}$$

where $\zeta(x)$ is the plane solitary-wave solution presented in Fig. 2(b) (the top figure). The initial data is perturbed by a long cosine function in the transverse direction and the subsequent evolution shows a focusing behavior which is arrested by the appearance of an elevation lump propagating with speed $c \approx 0.47$ behind the rest of the disturbance (see Fig. 3(c)), and the long-term evolution of the system is the formation of a group of lumps with small dispersions. This fact indicates that lumps are a global attractor of the BBL equation for a large class of initial conditions.

To validate our numerical algorithm, we compare the results of the ETDRK4 computations with those obtained from the method of integrating factors detailedly described in [29]. The averaged error at $t = 160$ between the two methods is of order 10^{-7}, providing a good verification for our codes. Figs. 3(e)–3(f) demonstrate the comparisons of x- and y-cross-sections between the resultant lump from the ETDRK4 method (dashed lines) and the exact traveling-wave solution obtained based on the Petviashvili scheme (solid line), which show remarkable agreement.

4.3. Collisions

As illustrated in the last section, plane solitary waves subject to long disturbances transverse to the direction of propagation eventually evolve into lumps. This fact indicates that elevation lumps are stable in the BBL equation and ulteriorly stimulates us to investigate lump interactions for understanding the 'soliton' properties of these solutions. For this purpose, the ETDRK4 algorithm proposed in Section 3 is applied with initial data being the superposition of two lumps of the BBL equation propagating with different velocities. We choose the computational domain, assumed periodic, and the initial location of lumps such that they have effectively decayed to zero within a reasonable distance of each other and the boundaries.

In the numerical experiments of head-on and overtaking collisions, a $30\pi \times 15\pi$ computational domain discretized with a 512×256 grid is adopted, and the time step Δt is set to 0.01. An example of the head-on collision is shown in Fig. 4, where waves move in opposite directions, towards each other, with their centers aligned. The interacting time between the two waves is so short that there appears to be no visible nonlinear effect except for very small oscillations shown in Fig. 4(c) resulting from small inelasticity of the collision. An example of the overtaking collision is shown in Fig. 5, where both waves move in the same direction with their centers aligned and the smaller (faster)

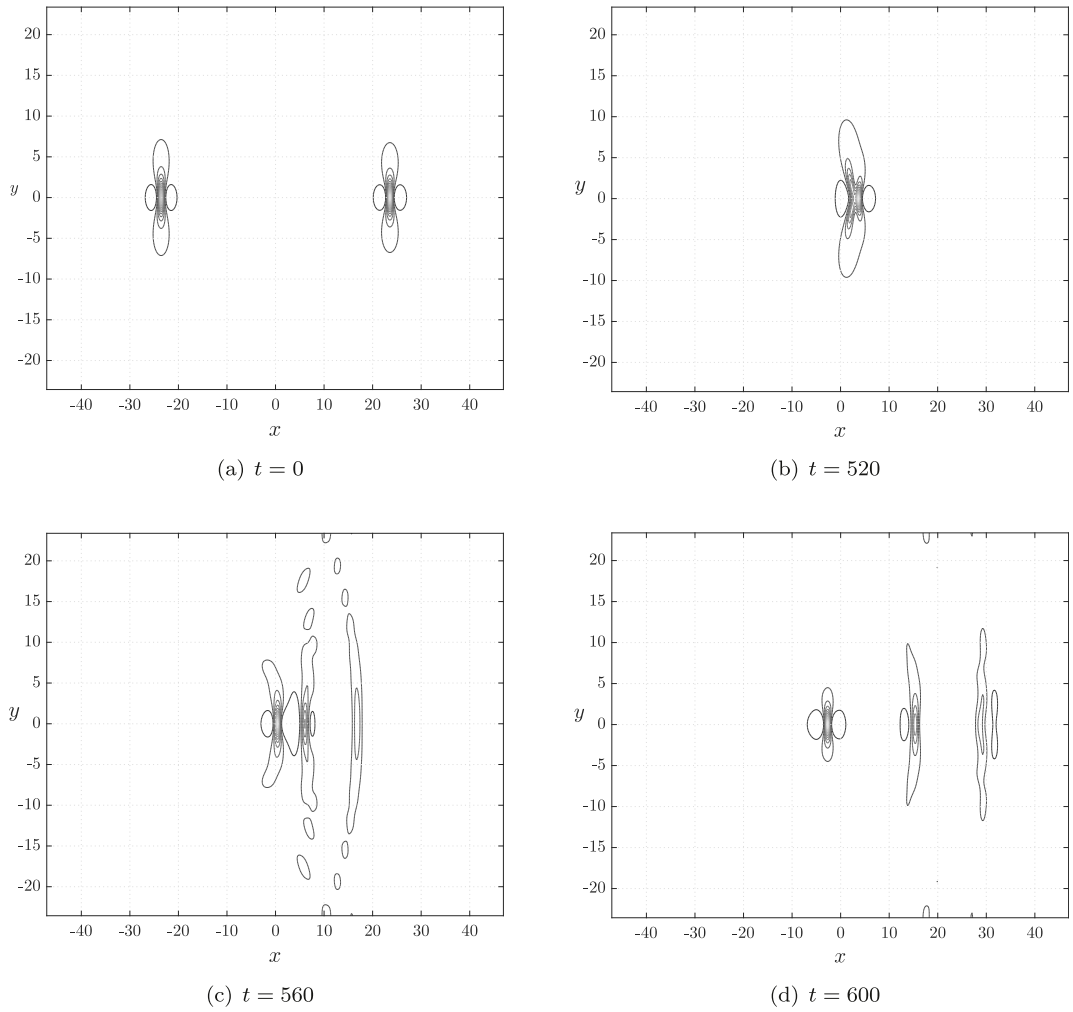

Fig. 5. Snapshots of an overtaking collision of lumps. The initial data are prepared by superposing two different lumps traveling in the same direction with the left one characterized by $c = 0.665$, $\|\eta\|_\infty = 11.89$ and the right one by $c = 0.59$, $\|\eta\|_\infty = 13.99$. The images are shown in a frame of reference moving to the right at the speed of the mean of two lumps. After the collision, there exists only one big lump with the amplitude of 14.70.

wave overtakes the larger (slower) one. The overtaking collision reveals considerable nonlinear interactions and only one big lump survives the collision which features a larger amplitude than both initial lumps and a radiated wave field.

Lumps can travel in any horizontal direction in an isotropic model equation, therefore it is interesting to collide two lumps obliquely. In an oblique collision, two lumps are initially placed on two sides of the x-axis with mirror symmetry and converge towards the axis at the incident angle of α. Fig. 6 shows contour plots of solution at different moments, where the angle $\alpha = 10°$ and the computational domain is $75\pi \times 150\pi$ discretized with a 512×1024 grid. Both solitary waves have the amplitude of 3.053 and the speed of 0.9139 in the direction of propagation. A smooth nonlinear interaction with lumps emerging intact after the collision can be observed in Fig. 6 and the phase shift phenomenon due to the nonlinear process is clearly shown in Fig. 7. The circles in Fig. 7 indicate the predicated location of the center of each lump from $t = 0$ to $t = 1650$, while the ×'s mark the actual computed location and illustrate the phase shift due to the collision, that is a phase lead of 10.02 in x and a phase lag of 33.94 in y at $t = 1650$. Given the grid resolution for this numerical experiment, $\Delta x = \Delta y = 0.46$, the measured phase shift is significant. If we change the incident angle α and the amplitude of lumps, there is no obvious phase shift in some computations. An example for this type of oblique collision is shown in Fig. 8, where $\alpha = 45°$, $\|\eta\|_\infty = 5.667$, and $c = 0.8485$. Two lumps of equal amplitude pass quickly through one another and produce no measurable phase shift, which may result from an insufficient energy exchange.

4.4. Generation of lumps by resonant flows beneath topography

In past decades, much attention has been paid to the generation and propagation of nonlinear waves due to external moving pressure. The conventional wisdom in this research field is to use the forced KdV and KP equations to study free-surface flows over variable bottom topography, and the interested readers are referred to [32] for a comprehensive review. In 3D pure gravity waves, Milewski & Tabak [29] numerically computed transient solutions to the generalized Benney–Luke equation at the critical speed of shallow water. Whereafter, Berger & Milewski [3] investigated the generation and evolution of lumps in surface-tension-dominated flows based on the modified Benney–Luke equation.

Since stable lumps exist in the free BBL equation, the next logical step is to study whether they can be generated when a uniform/non-uniform in time flow passes beneath a localized topography. We let $z = h + b(x, y, t)$ the top rigid lid, where h is constant and b is a function with compact support (a negative b corresponds to a downward

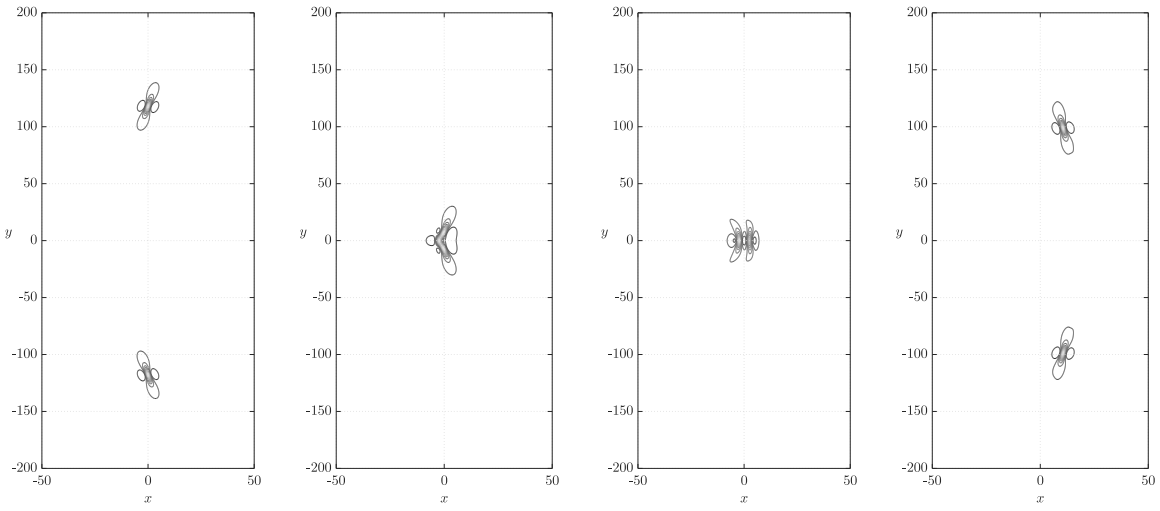

Fig. 6. An oblique collision between two lumps with equal amplitude traveling at the incident angle of 10° to the x-axis.

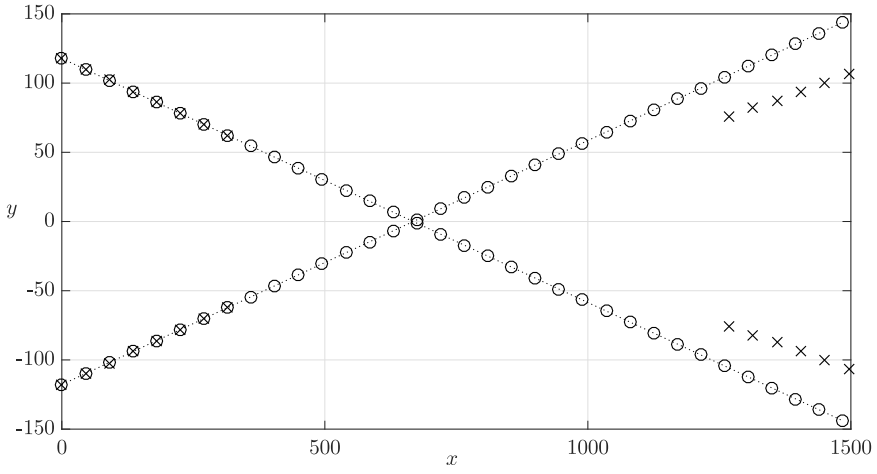

Fig. 7. The path of center of lumps of equal amplitude traveling from left to right at the incident angle of 10° to the x-axis. The circles indicate the predicated location of the center of each lump at $t = 50$ intervals from $t = 0$ to $t = 1650$ based on the solitary wave's known speed. The ×'s mark the actual computed location and illustrate the phase shift due to the collision. Tracking the center of each solitary wave is impossible in the interaction region.

bulge). Particularly, we assume that the prescribed function b is time dependent, therefore it can be used to model a uniform/non-uniform in time background current beneath a topography owing to the relativity of motion.

We discuss time-dependent solutions to Eq. (2.27) via the ETDRK4 algorithm. The first type of numerical experiments are carried out for a uniform flow beneath a topography. We assume a left-moving topography $b(x, y, t) = b(x + Ut, y)$ with constant speed U, which is equivalent to a uniform flow moving to the right and passing beneath a localized topography. All experiments are conducted in a $150\pi \times 80\pi$ domain discretize by a 1024×512 grid and the time step is set to 0.01. The non-dimensional parameters are chosen as follows: $\mu = 0.1$, $\epsilon = 0.1$, $B = 10$, and $R = 1.05$. The shape of the localized topography is described as a Gaussian function

$$b = -b_0 \exp\left[-\left(\frac{x^2}{9} + \frac{y^2}{16}\right)\right], \tag{4.4}$$

where b_0 is the height of topography and $b_0 = 0.2$ for Figs. 9 and 10. Since the velocity has been non-dimensionalized to unity to leading order, solutions to Eq. (2.27) can be divided into three categories: subcritical ($U < 1$), near-critical ($U \approx 1$), and supercritical ($U > 1$). In the subcritical regime, a steady elevation wave emanates from the described topography and transient waves moving off to the left as shown in Fig. 9(a) for $U = 0.5$. The numerical solution to Eq. (2.27) for a supercritical flow ($U > 1$) contains a steady waveform featuring a V-shaped pattern of wake lines (see Fig. 9(b) for $U = 1.5$). When the flow speed is close to the critical speed ($U \approx 1$), the phenomenon of periodic shedding of lumps occurs, and the underlying mechanism

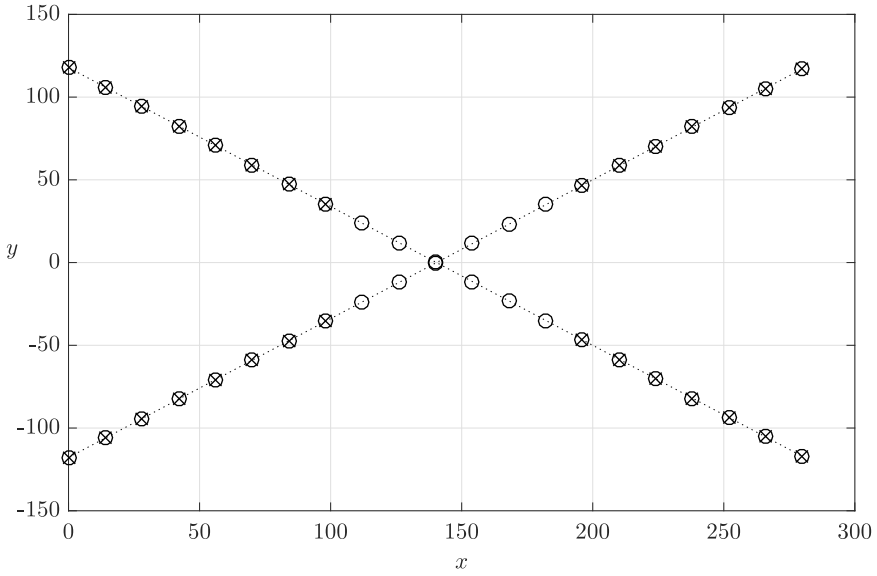

Fig. 8. The path of center of two lumps of equal amplitude traveling from left to right at the incident angle of 45°. The circles indicate the predicated location of the center of each lump at $t = 20$ intervals from $t = 0$ to $t = 400$ based on the solitary wave's known speed. The ×'s mark the actual computed location. Tracking the center of each soliton is impossible in the interaction region.

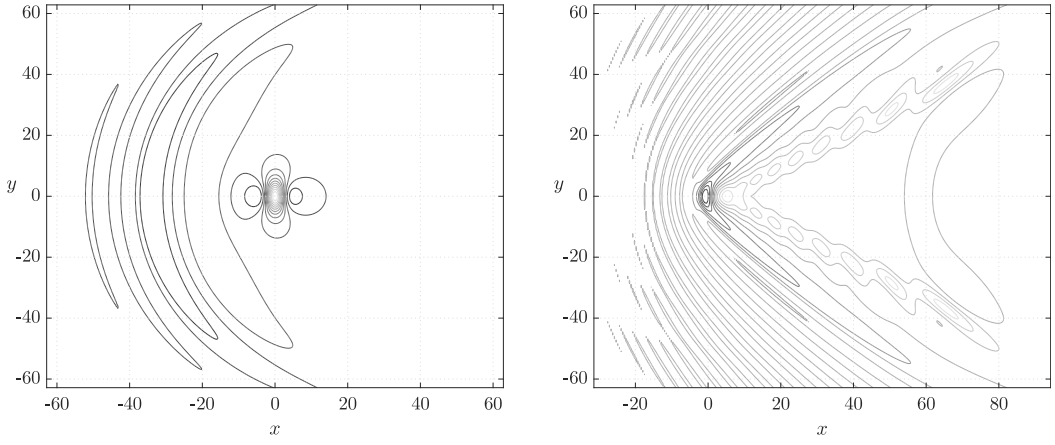

(a) $U = 0.5$ (b) $U = 1.5$

Fig. 9. (a) Uniform flow past a localized topography for $b_0 = 0.2$ and $U = 0.5$ at $t = 75$. (b) Uniform flow past a localized topography for $b_0 = 0.2$ and $U = 1.5$ at $t = 80$.

can be understood as follows. For a flow moving with a near-resonance speed, the energy accumulates locally near the topography, and as a consequence, the amplitude of the local wave grows. When the local wave reaches a certain threshold of magnitude, the nonlinear effects become sufficient and the subtle balance between weak nonlinearity and weak dispersion results in the formation of solitary waves propagating with velocities appropriate to their own amplitudes. The process is then repeated over a new cycle. A typical example for the time-periodic generation of lumps by a uniform flow moving at the near-critical speed ($U = 1$) beneath a localized topography is shown in Fig. 10.

It is well known that the nonlinearity, viscosity, and acceleration can suppress the unlimited increase in amplitude of waves at criticality based on linear theories. The second type of numerical experiments are carried out for a flow moving with constant acceleration. We first accelerate the velocity of the flow to $U = 1.2$ with a constant acceleration within a selected time period (for $t \in [0, 2000]$ say), and the flow moves with a constant speed afterwards. The most striking phenomenon is that though the flow is accelerated, the generation of lumps can also occur if the system can accumulate sufficient energy near criticality. A typical example is shown in Figs. 11 and 12 with $b_0 = 0.2$. The evolution of the interface displacement right below the center of topography is shown in Fig. 11 where three stages appear. The first stage is that $\eta(0, 0)$ grows sluggishly with speed in the subcritical regime, which generates a stable forced lump just like Fig. 9(a). However, in the second stage, the amplitude experiences a considerably sharp transition from rapid increase to quick decrease when the speed is in the transcritical regime,

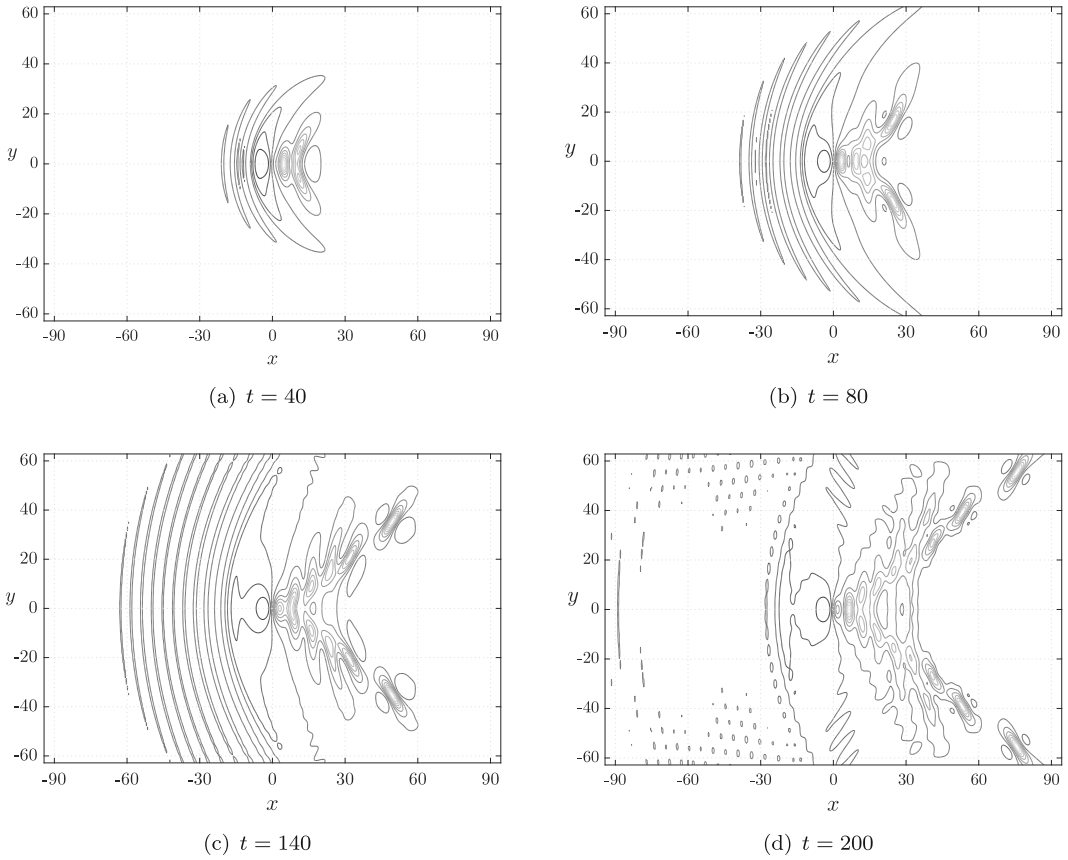

Fig. 10. Uniform flow past a localized topography for $b_0 = 0.2$ and $U = 1$ at $t = 40$, $t = 80$, $t = 140$, and $t = 200$.

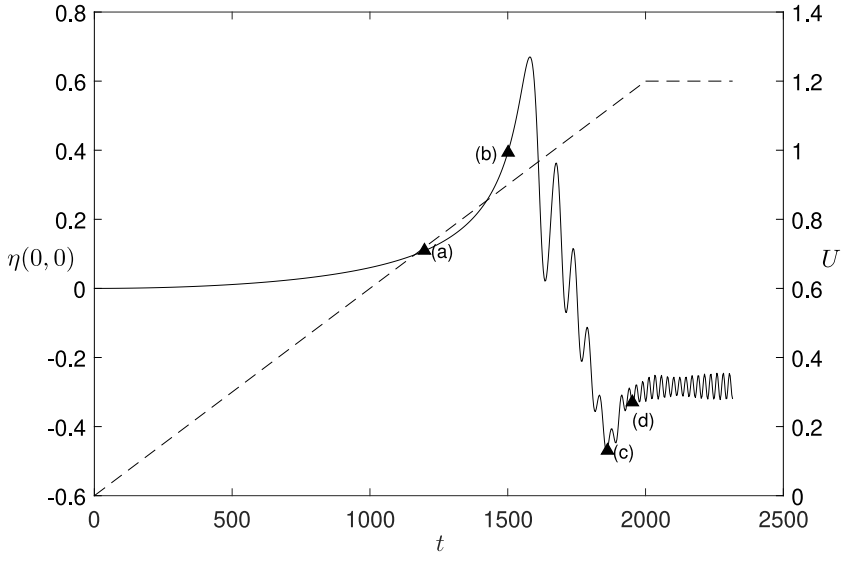

Fig. 11. The evolution of $\eta(0,0)$ (solid line) and the change of velocity (dashed line) as time varies. The velocity increases with a uniform acceleration for $t \in [0, 2000]$ and stays constant ($U = 1.2$) afterwards.

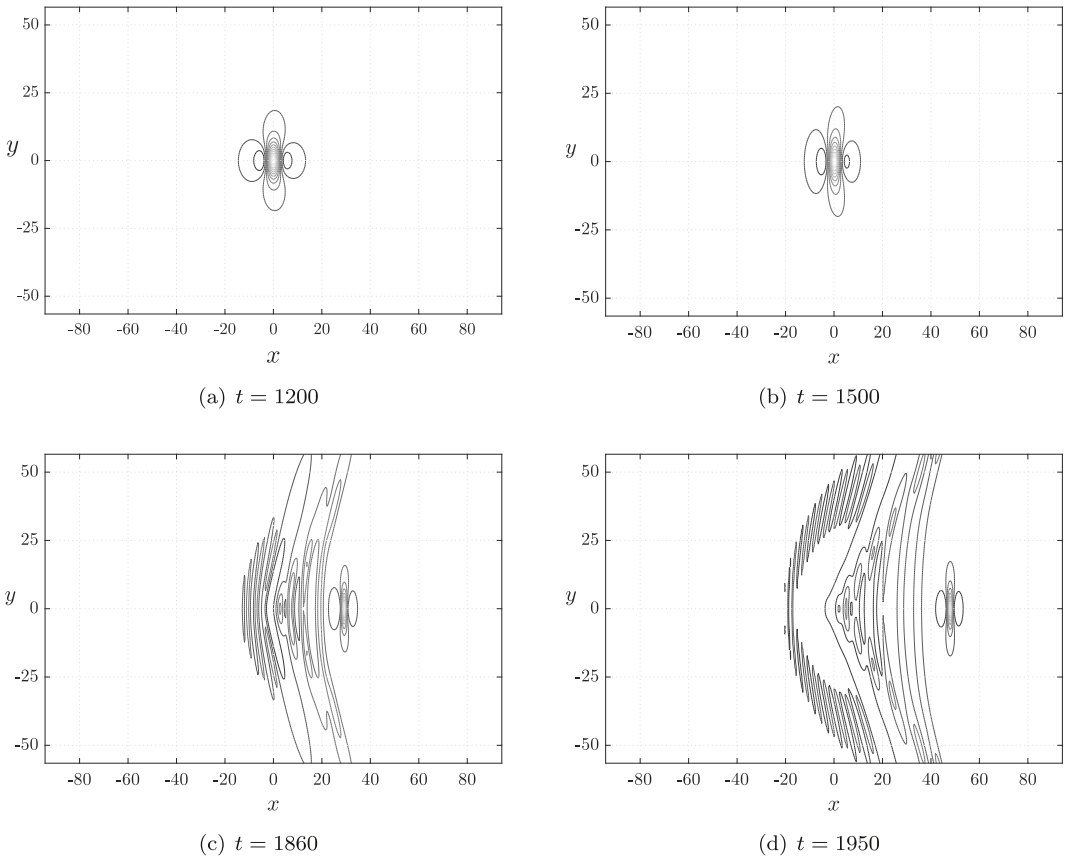

Fig. 12. Contour plots corresponding to (a)–(d) (marked with upper triangles shown in Fig. 11) for $t = 1200$, $t = 1500$, $t = 1860$, and $t = 1950$.

where the amplitude decrease is due to the energy release as the form of lump. The last stage is associated with the supercritical speed and stable state since we stop the acceleration process at $t = 2000$. The contour plots corresponding to (a)–(d) (marked with upper triangles in 11) are shown in Fig. 12. It should be noted that a lump has already been generated at $t = 1950$ before the acceleration is terminated. Increasing b_0 can lead to more complex behaviors and a typical example for $b_0 = 0.4$ is presented in Fig. 13. Due to more energy accumulations, three lumps generate in a sequence and lump C runs faster than lump B which results in an overtaking collision. The collision ultimately breaks up into two lumps moving along side by side, as shown in Fig. 13(c).

5. Conclusion

In the present paper, a weakly nonlinear model for long interfacial gravity–capillary waves in a two-layer system, which is the isotropic and bidirectional counterpart of the 2D Benjamin equation and termed the Benjamin–Benney–Luke equation, has been derived based on the Ablowitz–Fokas–Musslimani formulation. A detailed procedure of the ETDRK4 scheme, a numerical algorithm for solving stiff evolution PDEs, has been generalized and applied to the newly developed model equation with two spatial variables. Based on this algorithm, the existence and dynamics of gravity–capillary solitary waves in the BBL equation, including the transverse instability of plane solitary waves, lump collisions, and generation of lumps by resonant flow beneath a localized topography, have been thoroughly investigated. Qualitatively, some results of the BBL equation closely resemble those of the 2D Benjamin equation studied in [14]. Plane solitary waves are unstable subject to transverse disturbances of sufficiently long wavelength and evolve into stable elevation lumps. Three types of interactions between stable lumps, including the head-on, overtaking, and oblique collisions, are shown to be inelastic, indicating the imperfect 'soliton' property of lumps. When a localized topography on the rigid upper boundary is taken into consideration, we investigate solutions to Eq. (2.27) for flow beneath the topography with a uniform speed/acceleration. For a flow of uniform speed, solutions to the forced equation can be divided into three categories: subcritical ($U < 1$), near-critical ($U \approx 1$), and supercritical ($U > 1$). The near-critical regime is of great interest where nonlinear effects play an essential role giving rise to the time-periodic shedding of lumps due to the energy accumulation in a local fluid. Furthermore, it is found that lumps can also be generated when the flow moves with constant acceleration if the system can gain enough energy when the speed accelerates through the transcritical region.

Despite being of short wavelength, capillary–gravity lumps can be generated under controlled environment conditions in laboratories. Usually they are achieved by blowing air towards the surface of the fluid and moving the air source with speed close to the phase speed minimum (see [9–11] for more details). The computations in this paper provide another way to generate capillary–gravity lumps, that is, to move a localized topography on the rigid top lid of a two-layer fluid system with near-critical speed.

Acknowledgments

This work was supported by the National Natural Science Foundation of China (Nos. 11911530171, 11772341, 12132018) and the Strategic Priority Research Program of the Chinese Academy of Sciences (No. XDB22040203).

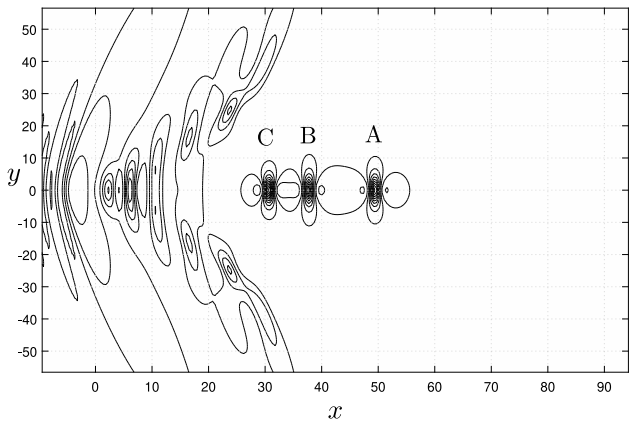

(a) $t = 1860$

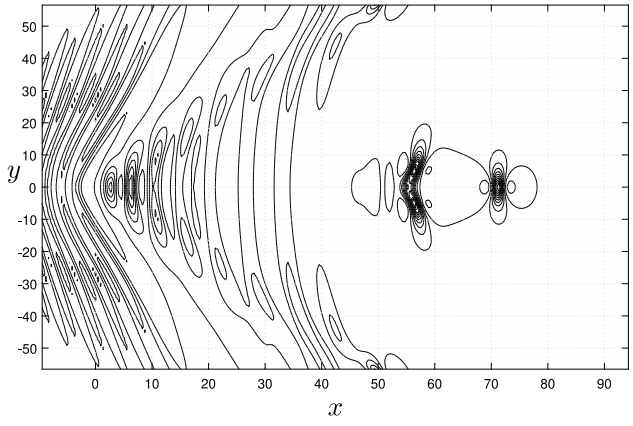

(b) $t = 1950$

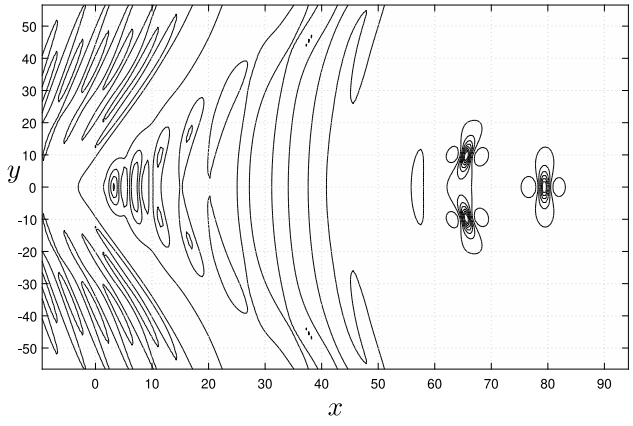

(c) $t = 1980$

Fig. 13. A uniformly accelerated flow past a localized topography for $b_0 = 0.4$. Contour plots are shown for $t = 1860$, $t = 1950$, and $t = 1980$, from top to bottom, respectively. Three lumps (labeled by A, B, and C) appear in sequence and move along the x-axis.

References

[1] Longuet-Higgins MS. Capillary–gravity waves of solitary type on deep water. J Fluid Mech 1989;200:451–70.

[2] Vanden-Broeck J-M, Dias F. Gravity-capillary solitary waves in water of infinite depth and related free-surface flows. J Fluid Mech 1992;240:549–57.

[3] Berger KM, Milewski PA. The generation and evolution of lump solitary waves in surface-tension-dominated flow. SIAM J Appl Math 2000;61(3):731–50.

[4] Părău EI, Vanden-Broeck J-M, Cooker MJ. Nonlinear three-dimensional gravity-capillary solitary waves. J Fluid Mech 2005;536:99–105.

[5] Kim B, Akylas TR. On gravity-capillary lumps. J Fluid Mech 2005;540:337–51.

[6] Akers B, Milewski PA. A model equation for wavepacket solitary waves arising from capillary–gravity flows. Stud Appl Math 2009;122(3):249–74.

[7] Wang Z, Milewski PA. Dynamics of gravity-capillary solitary waves in deep water. J Fluid Mech 2012;708:480–501.

[8] Milewski PA, Wang Z. Transversally periodic solitary gravity-capillary waves. Proc R Soc Lond Ser A Math Phys Eng Sci 2014;470:20130537.

[9] Diorio JD, Cho Y, Duncan JH, Akylas TR. Gravity–capillary lumps generated by a moving pressure source. Phys Rev Lett 2009;103:214502.

[10] Masnadi N, Duncan JH. Observations of gravity-capillary lump interactions. J Fluid Mech 2017;814(R1).

[11] Park B, Cho Y. Two-dimensional gravity-capillary solitary waves on deep water: generation and transverse instability. J Fluid Mech 2018;834:92–124.

[12] Benjamin TB. A new kind of solitary waves. J Fluid Mech 1992;245:401–11.

[13] Ambrose DM. Well-posedness of vortex sheets with surface tension. SIAM J Math Anal 2003;35(1):211–44.

[14] Kim B, Akylas TR. On gravity-capillary lumps. Part 2. Two-dimensional Benjamin equation. J Fluid Mech 2006;557:237–56.

[15] Calvo DC, Akylas TR. On interfacial gravity-capillary solitary waves of the Benjamin type and their stability. Phys Fluids 2003;15(5):1261–70.

[16] Kim B. Long-wave transverse instability of interfacial gravity-capillary solitary waves in a two-layer potential flow in deep water. J Eng Math 2009;65:325–44.

[17] Laget O, Dias F. Numerical computation of capillary–gravity interfacial solitary waves. J Fluid Mech 1997;349:221–51.

[18] Wang Z, Vanden-Broeck J-M, Meng H. A quasi-planar model for gravity-capillary interfacial waves in deep water. Stud Appl Math 2014;133(2):232–56.

[19] Benney DJ, Luke J. Interactions of permanent waves of finite amplitude. J Math Phys 1964;43:309–13.

[20] Ablowitz MJ, Fokas AS, Musslimani ZH. On a new non-local formulation of water waves. J Fluid Mech 2006;562:313–43.

[21] Curtis CW, Shen SSP. Three-dimensional surface water waves governed by the forced Benney-luke equation. Stud Appl Math 2015;135(4):447–65.

[22] Haut TS, Ablowitz MJ. A reformulation and applications of interfacial fluids with a free surface. J Fluid Mech 2009;631:375–96.

[23] Yuan C, Wang Z, Chen X. The derivation of an isotropic model for oceanic internal waves and its application to wave generation. Ocean Model 2020;153:101663.

[24] Beylkin G, Keiser JM, Vozovoi L. A new class of time discretization schemes for the solution of nonlinear PDEs. J Comput Phys 1998;147(2):362–87.

[25] Cox SM, Matthews PC. Exponential time differencing for stiff systems. J Comput Phys 2002;176(2):430–55.

[26] Kassam A, Trefethen LN. Fourth-order time-stepping for stiff PDEs. SIAM J Sci Comput 2005;26(4):1214–33.

[27] de la Hoz F, Vadillo F. An exponential time differencing method for the nonlinear Schrödinger equation. Comput Phys Commun 2008;179(7):449–56.

[28] Asgari Zohreh, Hosseini SM. Numerical solution of two-dimensional sine-Gordon and MBE models using Fourier spectral and high order explicit time stepping methods. Comput Phys Commun 2013;184:565–72.

[29] Milewski PA, Tabak EG. A pseudo-spectral procedure for the solution of nonlinear wave equations with example from free-surface flows. SIAM J Sci Comput 1999;21(3):1102–14.

[30] Kadomtsev BB, Petviashvili VI. On the stability of solitary waves in weakly dispersive media. Sov. Phys. Dokl 1970;15:539–41.

[31] Bridges TJ. Transverse instability of solitary-wave states of the water-wave problem. J Fluid Mech 2001;439:255–78.

[32] Akylas TR. Three-dimensional long water-wave phenomena. Ann Rev Fluid Mech 1994;26:191–210.